Three-Dimensional Trapping and Manipulation of a Mie Particle by Hybrid Acoustic Focused Petal Beams

Yan-Chun Luo,[1] Xin-Rui Li,[1] Da-Jian Wu,[1,†] Jie Yao,[1,2] Xing-Feng Zhu,[1,2] Liang-Fen Du,[3] and Xiao-Jun Liu[2,*]

[1] *Jiangsu Key Lab on Opto-Electronic Technology, School of Physics and Technology, Nanjing Normal University, Nanjing 210023, China*

[2] *MOE Key Laboratory of Modern Acoustics, School of Physics, Nanjing University, Nanjing 210093, China*

[3] *School of Mechanical and Aerospace Engineering, Nanyang Technological University, Singapore 639798, Singapore*

(Received 6 April 2022; revised 22 May 2022; accepted 24 May 2022; published 29 June 2022)

Acoustic manipulations of microparticles have significant implications in physics, chemistry, biology, and biomedicine. For large Mie particles, both the scattering force and the gradient force affect the trapping and manipulation behaviors, and thus, a passive acoustic tweezer (AT) for three-dimensionally manipulating a Mie particle remains challenging. Here, a passive AT based on a hybrid acoustic artificial plate is proposed to generate a hybrid acoustic focused petal beam (HAFPB) for capturing and manipulating a Mie microparticle in three dimensions. In the HAFPB, a lateral acoustic focused petal beam and an axial bifocal acoustic beam (BAB) combine to create a central zero-intensity zone for particle trapping, which can be adjusted by modulating the topological charge of the HAFPB. The acoustic radiation forces (ARFs) acting on large Mie particles with different diameters are investigated. The ARFs on the polystyrene sphere are greatly influenced by the particle size. If the particle is larger than the central zero-intensity zone, an AT with a larger topological charge and a stronger BAB is required for trapping and manipulating this larger particle. Finally, the experiments demonstrate that the AT can stably trap and manipulate a large Mie particle in three dimensions in water.

DOI: 10.1103/PhysRevApplied.17.064059

I. INTRODUCTION

Acoustic tweezers (ATs) have received a lot of attention and research interest because of their enormous potential applications in materials science [1], chemistry [2], and biomedicine [3]. Compared with other micromanipulation technologies [4,5], ATs have the advantages of no damage, good biocompatibility, label free, and long working distance [6–8], and thus, they have been used to directly manipulate particles, cells, and organisms [9–14]. In principle, there are two kinds of ATs, as determined from the method of production: the active AT [15,16] and the passive AT [17,18]. The active ATs are constructed from active emitters, including a single sound source with a certain geometry [19–21], several sound sources with a certain spatial arrangement [22,23], and a sound-source array [24]. They can realize predesigned acoustic fields by electrically controlling each sound source, which is used to trap and manipulate objects [25]. The active ATs can provide strong and tunable acoustic radiation forces (ARFs) but have the disadvantages of being expensive and large in size [26]. In the past decade, acoustic artificial structures, such as phononic crystals [27], metamaterials [28], metasurfaces [29], and artificial plates [30–35], have been explored to regulate incident sound fields and achieve ATs. Among them, the acoustic artificial plate (AAP) is an efficient, simple, and cheap method for modulating acoustic fields and manipulating objects [30–35]. For example, Xia *et al.* [33] reported an AAP carved with graded gratings that could deliver particles by adjusting the operating frequency. A silicon chip engraved with Archimedean spiral slits can convert the incident plane ultrasonic wave into a vortex beam, which is further used to manipulate particles and living shrimp eggs [31]. Zhou *et al.* [32] realized a position-adjustable bottle beam, the position of which could be controlled by modulating the operating frequency to axially move a single particle or bubble. An acoustic vortex beam with a twisted focus generated by a silicone binary-phase logarithmic spiral zone plate can achieve the three-dimensional spiral motion of a microparticle [35]. However, most previous passive ATs mainly realize the trappings and manipulations of small particles.

In general, the ARF includes the scattering force and gradient force [6,36,37]. For small particles, the acoustic scatterings from the particles are very weak, and hence,

*liuxiaojun@nju.edu.cn
†wudajian@njnu.edu.cn

the scattering force can be almost ignored [6,36,37]. Under these conditions, the trappings and manipulations of small particles can be achieved only by regulating incident sound fields. As the particle size is increased, the acoustic scattering of the particle is significantly enhanced, resulting in the improved scattering force [16,35]. As a result, while capturing and manipulating a bigger Mie particle, both scattering and gradient forces should be considered. Up to now, several passive ATs based on the acoustic vortex (AV) beam and acoustic petal beam with central zero-intensity zones were reported to achieve the trapping and manipulation of larger Mie particles in two dimensions [34]. However, the passive AT for three-dimensionally manipulating a large Mie particle in water remains a challenge.

Here, we design a hybrid acoustic artificial plate (HAAP) to generate a hybrid acoustic focused petal beam (HAFPB), which enables us to trap and manipulate a big Mie particle freely in three dimensions in water. The size of the zero-intensity zone at the center of the AT can be adjusted by changing the topological charge (TC) of the HAFPB, and accordingly, particles with different sizes can be trapped at the center. The influence of the size of the particle on the ARFs exerted on it by the AT is carefully investigated. Finally, we fabricate a HAAP and experimentally demonstrate the three-dimensional trapping and movement of a large PS particle in water using it.

II. HYBRID ACOUSTIC ARTIFICIAL PLATE FOR GENERATING A THREE-DIMENSIONAL ACOUSTIC TWEEZER

Figure 1 illustrates a schematic diagram of the proposed HAAP, which includes two parts: the outer combined Fresnel spiral slits (FSSs) and the inner bifocal Fresnel zone plate (BFZP). In Fig. 1(a), one M-arm anticlockwise FSS with an initial radius of r_1 is superimposed onto another M-arm clockwise FSS to form the combined FSS. The M-arm anticlockwise FSS can generate a focused acoustic vortex (FAV) with a TC of $l = M$, and the M-arm clockwise FSS produces a FAV with a TC of $l = -M$ [38]. When an acoustic plane wave with a wavelength of λ transmits through this combined FSS, two FAVs with opposite TCs of $l = \pm M$ are generated simultaneously, and the interaction between them results in a focused acoustic petal-like beam (FAPB) with $2M$ petals [39,40]. Here, the width of the slit is fixed at $d = \lambda/2$ and the focal length is set as f_1. Figure 1(b) shows a schematic of the inner BFZP consisting of two Fresnel zone plates (FZPs). The inner FZP with four concentric ring slits has a focal length of f_2 and the outer FZP with four concentric ring slits has a focal length of f_3 [41,42]. As an acoustic plane wave transmits through the BFZP, an axial bifocal acoustic beam (BAB) with two focal points of f_2 and f_3 can be formed. The initial radii of the inner and outer FZPs are r_{in} and r_{out}, respectively. The width of the nth slit can be obtained from [41,42]

$$
\begin{aligned}
T_{\text{in}}^{n} &= R_{\text{in}}^{n+1} - R_{\text{in}}^{n} = \sqrt{(\lambda + n\lambda/2 + f_2)^2 - f_2^2} \\
&\quad - \sqrt{[\lambda + (n-1)\lambda/2 + f_2]^2 - f_2^2}, \\
T_{\text{out}}^{n} &= R_{\text{out}}^{n+1} - R_{\text{out}}^{n} = \sqrt{(2.4\lambda + n\lambda/2 + f_3)^2 - f_3^2} \\
&\quad - \sqrt{[2.4\lambda + (n-1)\lambda/2 + f_3]^2 - f_3^2}. \qquad (1)
\end{aligned}
$$

Here, $n = 1$, 2, 3, and 4. The HAAP is constructed by surrounding the BFZP with the combined FSS, as shown in Fig. 1(c). When an acoustic plane wave transmits through this HAAP, both the lateral AFPB and the axial BAB constitute a zero-intensity zone at the center of the AT for trapping objects.

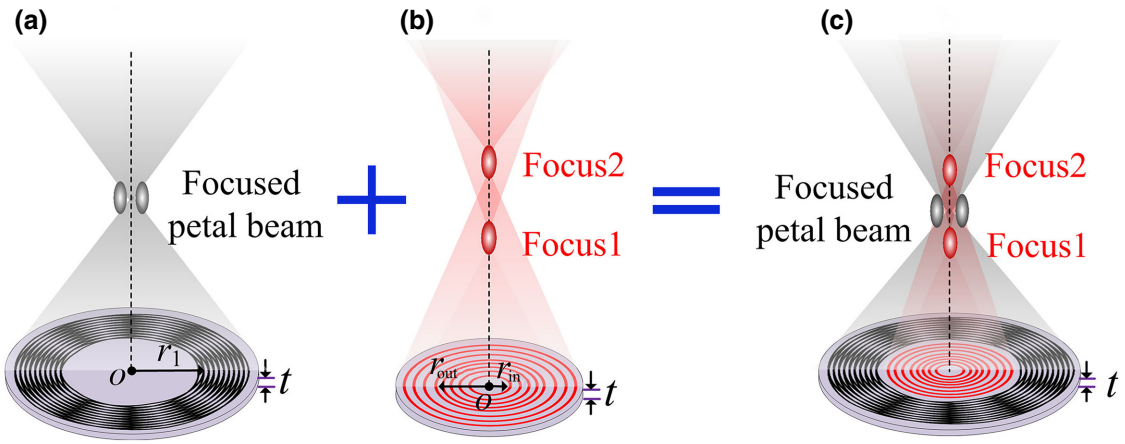

FIG. 1. (a) Schematic diagram of the combined FSSs for producing a lateral AFPB. (b) Schematic diagram of the BFZP for generating an axial BAB. (c) Schematic diagram of the HAAP for realizing the AT.

Figure 2 shows the normalized analytical acoustic intensity and phase distributions of two ATs in water based on the Rayleigh-Summerfield diffraction integral [43–45]. Throughout this work, the working frequency is fixed at 1 MHz. Figure 2(a1) depicts the structure of the HAAP for generating a smaller AT with $l=2$. The outer combined FSS with $r_1 = 8\sqrt{3}\lambda$ produces an AFPB with $2l=4$ petals and the focal-plane local $z=f_1=8\lambda$. Meanwhile, the inner BFZP with $r_{\text{in}} = 3\lambda$ and $r_{\text{out}} = 4\sqrt{3.96}\lambda$ generates two focal points at $z=f_2=4\lambda$ and $z=f_3=12\lambda$. Figure 2(a2) shows the three-dimensional (3D) view of the acoustic intensity distribution of the AT with $l=2$. Figures 2(a3) and 2(a4) represent the acoustic intensity and phase profiles on three focal planes of $z=12\lambda$, $z=8\lambda$, and $z=4\lambda$, respectively. At $z=f_1=8\lambda$, four petal-like bright spots are observed in the intensity distribution, and the phase profile is divided into four sections with an adjacent jump of π [34,40]. At the same time, two bright spots appear at two focal points of (0, 0, 12λ) and (0, 0, 4λ). Both the lateral AFPB and the axial BAB construct a zero-intensity region, as shown in Fig. 2(a2), which is expected to be used to trap objects. Figure 2(b1) describes the structure of the HAAP for a larger AT with $l=5$. The design of the BFZP is consistent with that of Fig. 2(a1), and it can produce two focal points at (0, 0, 12λ) and (0, 0, 4λ). The outer combined FSS with $r_1 = 8\sqrt{3}\lambda$ produces two FAVs with $l=\pm5$, and the coupling between them realizes an AFPB with ten petals on the focal plane of $z=f_1=8\lambda$. Figure 2(b2) shows the 3D view of the acoustic intensity distribution of the AT with $l=5$. Figures 2(b3) and 2(b4) show the corresponding acoustic intensity and phase distributions at three focal planes of $z=12\lambda$, $z=8\lambda$, and $z=4\lambda$, respectively. At $z=12\lambda$ and $z=4\lambda$, the two focal points are clearly observed. At $z=8\lambda$, the flowerlike intensity pattern with ten bright petals is observed, and the corresponding phase profiles are split into ten sectors with a phase shift of π. It is obvious that the central zero-intensity region of the larger AT is larger than that of the smaller AT.

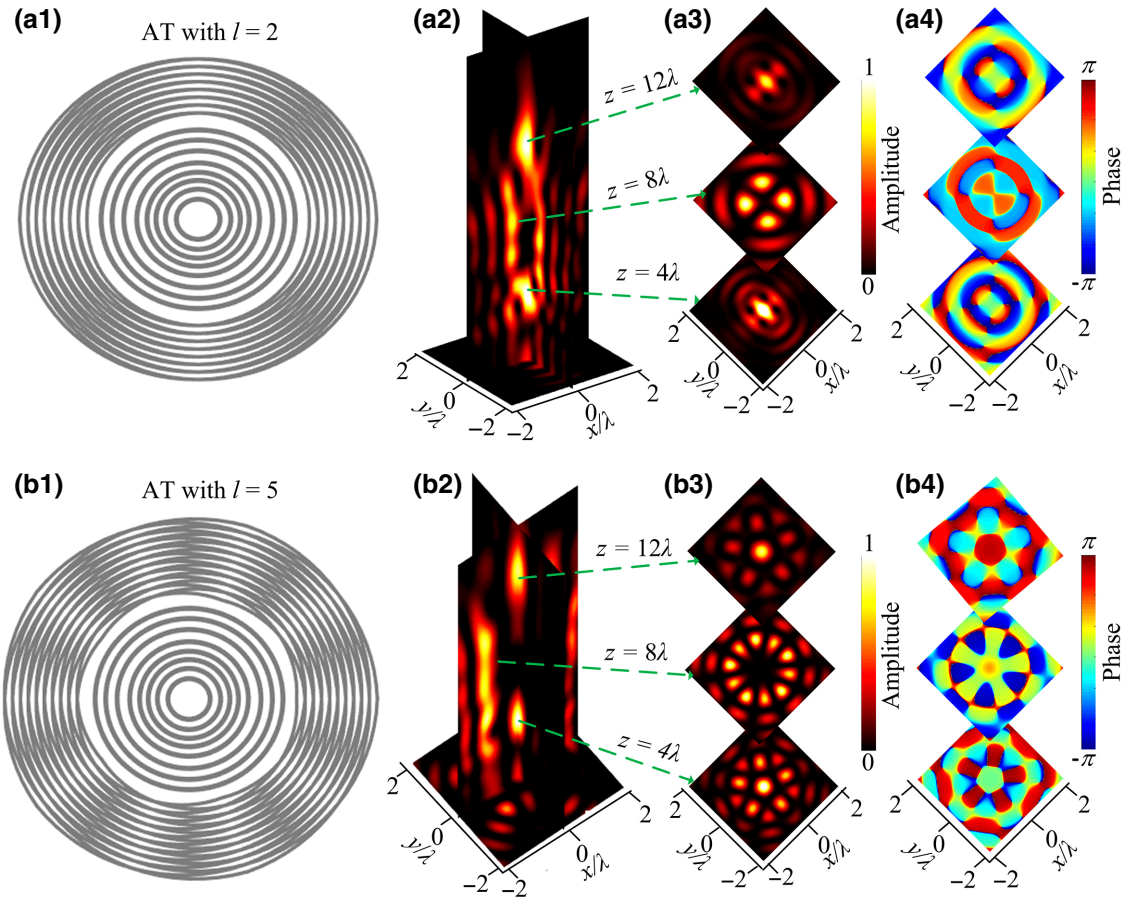

FIG. 2. (a1) Schematic diagram of a HAAP for a smaller AT with $l=2$. (a2) Three-dimensional view of the normalized acoustic intensity distribution of the smaller AT. Normalized acoustic (a3) intensity and (a4) phase distributions of the smaller AT in three focal planes of $z=12\lambda$, 8λ, and 4λ. (b1) Schematic diagram of a HAAP for a larger AT with $l=5$. (b2) Three-dimensional view of the normalized acoustic intensity distribution of the larger AT. Normalized acoustic (b3) intensity and (b4) phase distributions of the larger AT in three focal planes of $z=12\lambda$, 8λ, and 4λ.

III. NUMERICAL SIMULATIONS FOR ACOUSTIC FIELD DISTRIBUTIONS AND ACOUSTIC RADIATION FORCES OF ACOUSTIC TWEEZERS

We perform simulations based on the finite-element model (using business software COMSOL Multiphysics) to verify the above theoretical predictions. The material of the HAAP is set as acoustically rigid and the surrounding medium is water with a density of $\rho_0 = 1000$ kg/m^3 and sound velocity of $c_0 = 1500$ m/s. Figure 3(a) shows the normalized simulated acoustic intensity distributions of the smaller AT with $l = 2$ in the x-z plane and in three focal planes of $z = 12\lambda$, $z = 8\lambda$, and $z = 4\lambda$. The corresponding results of the larger AT with $l = 5$ are displayed in Fig. 3(b). The simulated acoustic intensity distributions of two ATs agree well with the analytical results in Fig. (2). In addition, we calculate the potentials of a Rayleigh polystyrene (PS) particle in two ATs by means of Gor'kov potential theory [6,34,36,37]. Figures 3(c) and 3(d) represent the simulated potential distributions of two ATs in the x-z plane and in three focal planes of $z = 12\lambda$, $z = 8\lambda$, and $z = 4\lambda$. The arrows indicate the negative spatial gradient of the Gor'kov potential. Here, the amplitude and frequency of incident acoustic waves are 10^6 Pa and 1.0 MHz, respectively, and the diameter of the Rayleigh PS sphere is 0.24 mm ($\sim 0.16\lambda$). In Fig. 3(c), a potential valley appears at the center of the smaller AT, and the ARFs are directed toward the center. Therefore, the particle near the central valley can be restricted in this potential valley and the particle initially outside the central valley will be repelled away. For the larger AT with $l = 5$, a three-dimensional potential valley is also found at the center and its size becomes larger, as shown in Fig. 3(d).

Furthermore, we focus on the manipulation of the larger Mie particle using the larger AT. It is well known that the ARFs exerted on a large Mie particle are related to not only the sound-field distribution but also the scattering of the particle. With increasing particle size, the scattering of the particle is enhanced and becomes complicated. To evaluate the feasibility of the larger AT for three-dimensional stable manipulation of a Mie particle, a larger PS sphere is introduced into the finite-element model of the AT with $l = 5$, and the ARFs acting on PS spheres with different sizes are calculated. Figure 4(a1) shows the normalized simulated acoustic intensity distribution of the AT with $l = 5$ in the x–z plane, where a PS sphere with a diameter of 0.6 mm ($\sim 0.4\lambda$) is placed at the center. Figure 4(a2) shows the axial ARF in the z-direction F_z acting on the PS particle. F_z exhibits a negative force gradient in the region of $z = [\sim 4.71\lambda, \sim 6.23\lambda]$ and $F_z = 0$ is found at $z \approx 6.0\lambda$. In the z direction, the axial ARF F_z, gravity G, and buoyancy force F_b of the particle should be all considered. The gravitational acceleration g is set as about 9.8 m/s^2. The density of the PS sphere is $\rho_s = 1100$ kg/m^3, and $c_l = 2170$ m/s and $c_t = 1100$ m/s are the longitudinal and transverse sound velocities, respectively. For the PS sphere with a diameter of 0.6 mm ($\sim 0.4\lambda$), gravity and the buoyancy force are about 1.22×10^{-6} and 1.11×10^{-6} N, respectively. The difference between gravity and the buoyancy force is defined as $F_c = (G - F_b) = \sim 1.11 \times 10^{-7}$ N, which is displayed as the dashed line in Fig. 4(a2). In this case, we can find a position range in the z direction where the negative F_z exerted on the particle can overcome F_c. Figure 4(a3) shows the lateral ARF in the x-direction F_x. It is observed that F_x exhibits a positive force gradient within the range of $x = [-0.7\lambda, 0.5\lambda]$. The ARF with a positive force gradient indicates that the PS sphere will be pushed out of the center [46]. Thus, the PS sphere with a diameter of 0.6 mm ($\sim 0.4\lambda$) cannot be stably trapped by the AT with $l = 5$. Figure 4(b1) shows the normalized simulated acoustic intensity distribution of the larger AT with a PS sphere with a diameter of 0.75 mm (0.5λ) at its center. Figure 4(b2) shows the axial ARF F_z acting on the PS particle in the z direction. It is found that $F_z = 0$ appears at $z \approx 6.4\lambda$ and exhibits a negative force gradient around $z = 6.4\lambda$. Gravity and the buoyancy force of the particle are about 2.38×10^{-6} and 2.16×10^{-6} N, respectively, and hence, $F_c = \sim 2.16 \times 10^{-7}$ N (dashed line). We also can find a position range in the z direction where the negative F_z exerted on the particle can overcome F_c [47]. In Fig. 4(b3), the lateral ARF F_x shows a negative force gradient in the region of $[-0.6\lambda, 0.\ 6\lambda]$, and $F_x = 0$ appears at $x \approx 0$. Here, $z = 6.4\lambda$. The lateral ARF with a negative force gradient means that the PS particle can be pushed to the zero point of ARF [34,36]. Therefore, this PS particle with a diameter of 0.75 mm (0.5λ) can be trapped by the AT. Figure 4(c1) shows the simulated acoustic intensity distribution of the AT where a PS sphere with a diameter of 1.5 mm (λ) is placed at the center. Figure 4(c2) shows the calculated F_z exerted on the PS sphere. F_z exhibits a negative force gradient in the region of $z \approx [4.71\lambda, 8.13\lambda]$ and $F_z = 0$ is found at $z \approx 7.0\lambda$. Gravity and the buoyancy force of the particle are about 1.91×10^{-5} and 1.73×10^{-5} N, respectively, and hence, $F_c = \sim 1.73 \times 10^{-6}$ N (dashed line). We still can find a position range in the z direction where the negative F_z exerted on the particle can overcome F_c. In Fig. 4(c3), F_x represents the negative force gradient in $x \approx [-0.299\lambda, 0.3\lambda]$, and $F_x = 0$ appears at $x \approx 0$. Here, $z = 7.0\lambda$. In this case, the size of the PS particle is still smaller than the central zero-intensity region, and the PS sphere can also be stably trapped by the AT. We further increase the diameter of the PS sphere to 2.5 mm ($\sim 1.67\lambda$), as shown in Fig. 4(d1). Under these conditions, the axial ARFs, F_z, shown in Fig. 4(d2) are all positive. Since there is no negative F_z to overcome F_c, the particle is unstable in the axial direction. Meanwhile, the lateral ARFs, F_x, exerted on the PS particle exhibit a positive force gradient around the center of the AT, which indicates that this PS

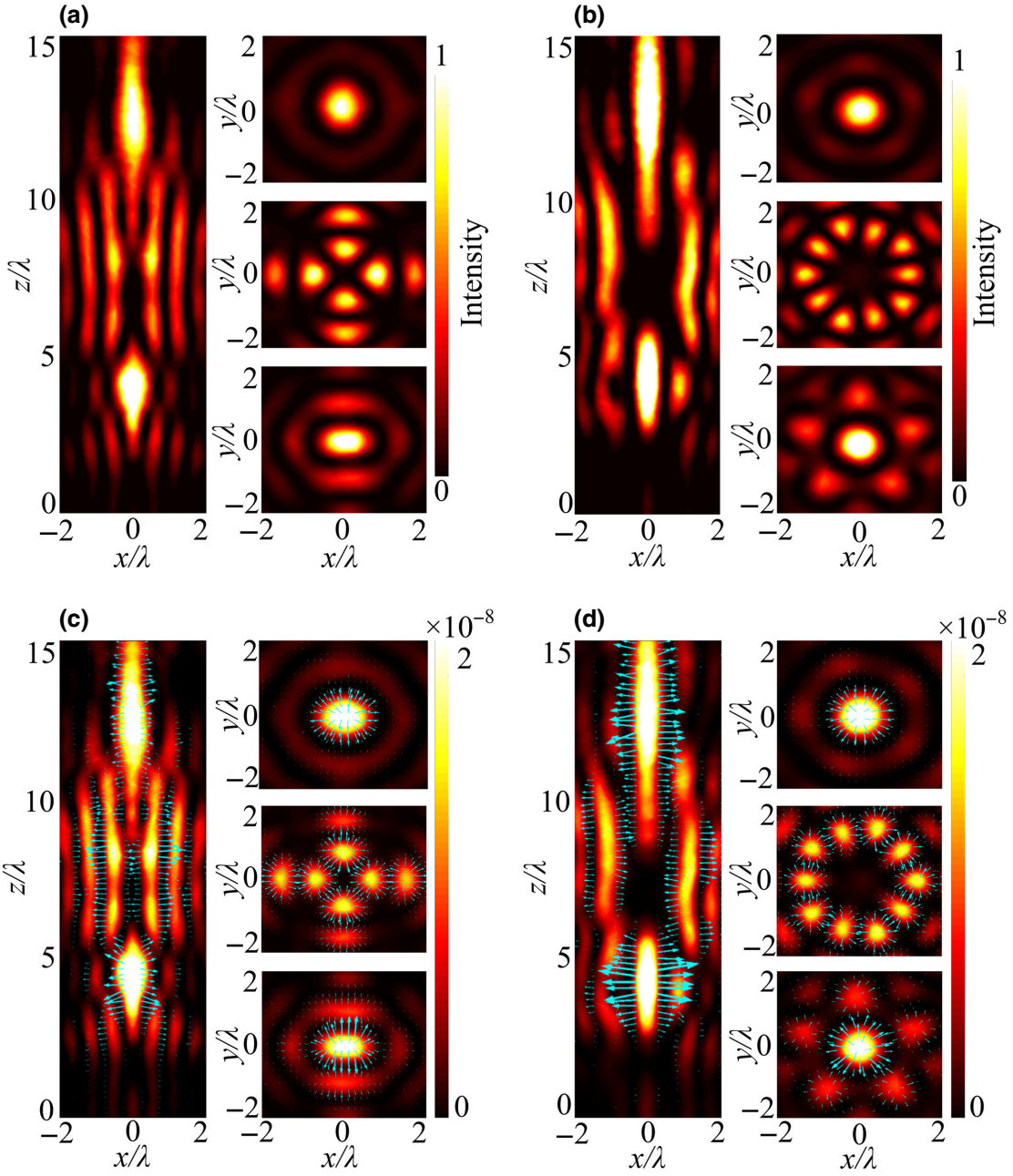

FIG. 3. (a) Normalized simulated acoustic intensity distributions of the smaller AT with $l=2$ in the x-z plane and on three focal planes of $z=12\lambda$, $z=8\lambda$, and $z=4\lambda$. (b) Normalized simulated acoustic intensity distributions of the larger AT with $l=5$ in the x-z plane and on three focal planes of $z=12\lambda$, $z=8\lambda$, and $z=4\lambda$. (c) Simulated Gor'kov potentials of the smaller AT in the x-z plane and on three focal planes of $z=12\lambda$, $z=8\lambda$, and $z=4\lambda$. (d) Simulated Gor'kov potentials of the larger AT in the x-z plane and on three focal planes of $z=12\lambda$, $z=8\lambda$, and $z=4\lambda$. Arrows indicate the negative spatial gradient of the Gor'kov potential.

sphere cannot be captured by the AT. Therefore, when the size of the particle is larger than the size of the central zero-intensity region of the AT, the stable trapping of the PS particle using the AT with $l=5$ is impossible. Furthermore, as described in detail in the Supplemental Material [48], we carefully study the lateral ARF, F_x, and axial ARF, F_z, exerted on more PS spheres with different diameters. The results reveal that the AT with a TC of five can three-dimensionally capture the PS spheres with suitable sizes. For the larger particle, an AT with a larger TC and a stronger BAB is required.

IV. EXPERIMENTS FOR THREE-DIMENSIONALLY TRAPPING AND MANIPULATING A MIE PARTICLE

Finally, we fabricate the HAAP to generate a larger AT with $l=5$ and use it to three-dimensionally

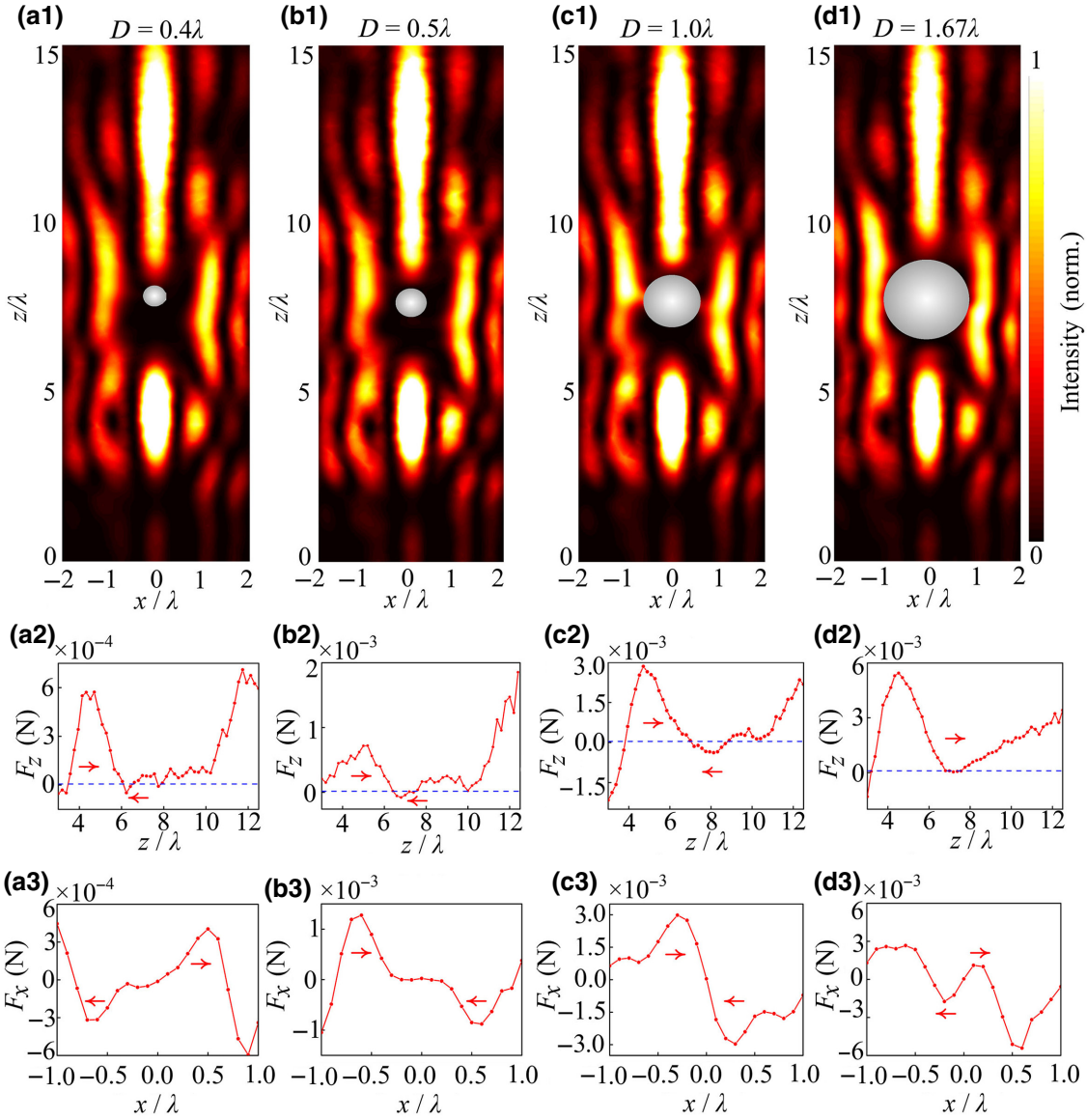

FIG. 4. Normalized simulated acoustic intensity distribution of the larger AT with $l = 5$ in the x-z plane, where a PS sphere with a diameter of (a1) 0.6 mm (0.4λ), (b1) 0.75 mm (0.5λ), (c1) 1.5 mm (1.0λ), and (d1) 2.5 mm (1.67λ) is placed at the center. F_z exerted on the PS sphere with a diameter of (a2) 0.6 mm (0.4λ), (b2) 0.75 mm (0.5λ), (c2) 1.5 mm (1.0λ), and (d2) 2.5 mm (1.67λ) by the larger AT. F_x exerted on the PS sphere with a diameter of (a3) 0.6 mm (0.4λ), (b3) 0.75 mm (0.5λ), (c3) 1.5 mm (1.0λ), and (d3) 2.5 mm (1.67λ) by the larger AT.

manipulate a larger Mie particle. The working frequency is set as 1 MHz. Figure 5(a) shows a photograph of the HAAP sample. The FSS with $r_1 = 8\sqrt{3}\lambda = 20.78$ mm and the BFZP with $r_{\text{in}} = 3\lambda = 4.5$ mm and $r_{\text{out}} = 4\sqrt{3.96}\lambda = 11.94$ mm are engraved on a square of stainless steel ($120 \times 120 \times 1.0$ mm) using the laser-etching technique. Here, the width of the slit of the FSS is fixed at $d = 0.75$ mm. Actually, the effective area on the stainless-steel HAAP is a central circular region with a diameter of about 7.5 cm. The density, longitudinal wave speed, and shear wave speed of stainless steel are $\rho = 7900$ kg/m^3, $c_L = 5240$ m/s, and $c_T = 2978$ m/s, respectively [44]. To enhance structural stability and for easier fabrication, radial bars with a width of 8 mm are added to the sample. The influence of these additional radial bars on the AT and ARF is carefully discussed in the Supplemental Material [48]. Figure 5(b) shows the normalized simulated acoustic intensity distribution generated by the modified HAAP shown in Fig. 5(a), which is in accordance with those shown in Figs. (2) and (3). Therefore, the additional radial bars have almost no influence on the acoustic field of the AT. In the manipulation experiment, an ultrasound transducer with a central frequency of 1.0 MHz connected with the x-y-z translation platform is placed in a water

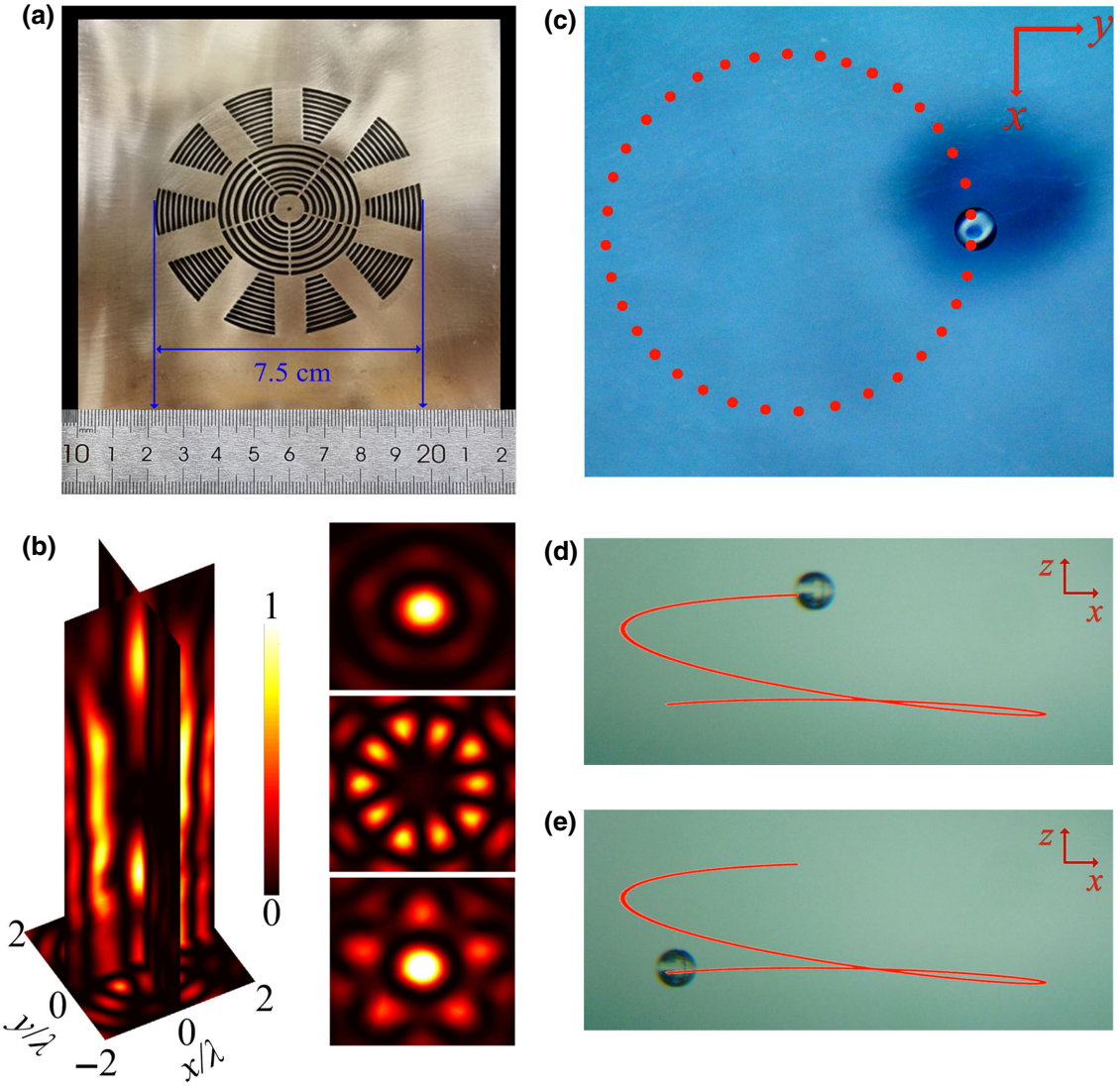

FIG. 5. (a) Photographs of the modified steel HAAP sample for the larger AT with $l = 5$. (b) Simulated three-dimensional acoustic intensity distribution of the modified HAAP and the corresponding acoustic intensity distribution in three focal planes of $z = 12\lambda$, 8λ, and 4λ. (c) Photograph of the Mie PS particle suspended in water, which will move along a circular path in the x-y plane. Pictures of the Mie PS particle at (d) beginning and (e) end positions of the three-dimensional spiral motion.

tank and the HAAP sample is placed below the transducer by a clamp holder. Several PS spheres with a diameter of about 0.75 mm ($\sim 0.5\lambda$) are placed on a culture dish. Two digital cameras are mounted below and to one side of the water tank to record the movements of the particle. After the sound source is turned on, sound waves from the transducer pass through the HAAP sample to form the larger AT. We first use the AT to trap a PS sphere on the culture dish and then move the AT so that this PS sphere is suspended in the water tank. Next, this PS sphere is manipulated to move along a circular path in the x-y plane, as indicated in Fig. 5(c) (see multimedia video 1 within the Supplemental Material [48]). Furthermore, we manipulate the AT to move this PS particle along a three-dimensional spiral path. Figures 5(d) and 5(e) show photographs of the suspended PS particle at the beginning and end positions of the three-dimensional spiral path. The three-dimensional spiral motion behavior of this PS sphere is recorded by the digital camera (see multimedia video 2 within the Supplemental Material [48]). Therefore, we experimentally demonstrate that the proposed AT can trap and manipulate a large PS particle in water in three dimensions. In addition, we study the trapping and rejecting behaviors of PS spheres with different sizes by the AT with a TC of five. In multimedia video 3 within the Supplemental Material [48], a PS sphere with a diameter of about 0.6 mm ($\sim 0.4\lambda$) is first placed on a culture dish and at the center of the HAAP. The culture dish has no influence on the acoustic field distributions and the particle manipulations in experiments [34]. The distance between

the HAAP and the culture dish is set as about 6.4λ. When an acoustic plane wave is launched on the HAAP, the PS sphere is immediately ejected from the center of the AT, and it does not move with the AT. Next, a PS sphere with a diameter of about 0.75 mm (∼0.5λ) is placed near the center of the HAAP. As the transducer is turned on, the PS microsphere is immediately captured at the center of the AT, and then it moves with the AT. In multimedia video 4 within the Supplemental Material [48], two PS microspheres with diameters of about 0.6 mm (∼0.4λ) and 1.5 mm (∼λ) are placed near the center of the HAAP. As the transducer is turned on, the larger PS microsphere is immediately captured at the center of AT, and then it moves with the AT. Meanwhile, the smaller PS microsphere is ejected from the center of the AT.

V. CONCLUSIONS

We propose an AT based on the well-designed HAAP, which can realize the three-dimensional stable trapping and manipulation of larger Mie particles in water. The HAAP consists of an outer combined FSS and an inner BFZP, which generate a lateral AFPB and an axial BAB, respectively. The AFPB and BAB together construct an AT with a central zero-intensity zone, and its size can be adjusted by modulating the TC of the AFPB. In the potential distributions of the smaller and larger ATs, a 3D potential valley appears at the centers of two ATs and the ARFs on the particles are directed toward the centers. Furthermore, the lateral and axial ARFs acting on the PS spheres with different sizes by the larger AT with $l = 5$ are studied carefully. It is found that the size of the particle has a great influence on the ARFs, and the AT with $l = 5$ can trap and manipulate the PS sphere with a suitable size. The trapping and manipulation of a larger particle requires an AT with a larger l. Finally, we fabricate the HAAP for a larger AT with $l = 5$ and experimentally demonstrate that this AT can stably trap and three-dimensionally manipulate a Mie PS particle in water. Our AT may hopefully become a useful tool for the three-dimensional manipulation of larger objects in particle transport, biomedical analysis, or targeted drug delivery.

ACKNOWLEDGMENTS

This work is supported by the National Natural Science Foundation of China under (Grants No. 11874222, No. 12027808, No. 12074191, and No. 12174197) and the Postgraduate Research & Practice Innovation Program of Jiangsu Province (Grant No. KYCX21_1321).

[1] S. Polychronopoulos and G. Memoli, Acoustic levitation with optimized reflective metamaterials, Sci. Rep. **10**, 4254 (2020).

[2] S. Santesson and S. Nilsson, Airborne chemistry: Acoustic levitation in chemical analysis, Anal. Bioanal. Chem. **378**, 1704 (2004).

[3] M. X. Wu, Y. S. Ouyang, Z. Y. Wang, R. Zhang, P. Huang, C. Chen, H. Li, P. Li, D. Quinn, M. Dao, S. Suresh, Y. Sadovsky, and T. J. Huang, Isolation of exosomes from whole blood by integrating acoustics and microfluidics, Proc. Natl. Acad. Sci. U. S. A. **114**, 10584 (2017).

[4] K. Svoboda and S. M. Block, Biological applications of optical forces, Annu. Rev. Biophys. Biomol. Struct. **23**, 247 (1994).

[5] K. C. Neumaan and A. Nagy, Single-molecule force spectroscopy: Optical tweezers, magnetic tweezers and atomic force microscopy, Nat. Meth. **5**, 491 (2008).

[6] D. Baresch, J. L. Thomas, and R. Marchiano, Observation of a Single-Beam Gradient Force Acoustic Trap for Elastic Particles: Acoustic Tweezers, Phys. Rev. Lett. **116**, 024301 (2016).

[7] V. Marx, Biophysics: Using sound to move cells, Nat. Meth. **12**, 41 (2015).

[8] D. Baresch, J. L. Thomas, and R. Marchiano, Three-dimensional acoustic radiation force on an arbitrarily located elastic sphere, J. Acoust. Soc. Am. **133**, 25 (2013).

[9] T. Laurell, F. Petersson, and A. Nilsson, Chip integrated strategies for acoustic separation and manipulation of cells and particles, Chem. Soc. Rev. **36**, 492 (2007).

[10] W. J. Xie, C. D. Cao, Y. J. Lü, Z. Y. Hong, and B. Wei, Acoustic method for levitation of small living animals, Appl. Phys. Lett. **89**, 214102 (2006).

[11] D. G. B. aresch, J. L. Thomas, and R. G. Marchiano, Orbital Angular Momentum Transfer to Stably Trapped Elastic Particles in Acoustical Vortex Beams, Phys. Rev. Lett. **121**, 074301 (2018).

[12] H. D. Zhu, P. R. Zhang, Z. W. Zhong, J. P. Xia, J. Rich, J. H. Mai, X. Y. Su, Z. H. Tian, H. T. Bachman, J. Rufo, Y. Y. Gu, P. T. Kang, K. S. D. Chakrabarty, T. P. Witelski, and T. J. Huang, Acoustohydrodynamic tweezers via spatial arrangement of streaming vortices, Sci. Adv. **7**, eabc7885 (2021).

[13] R. B. Lirette, J. Mobley, and L. K. Zhang, Ultrasonic Extraction and Manipulation of Droplets from a Liquid-Liquid Interface with Near-Field Acoustic Tweezers, Phys. Rev. Appl. **12**, 061001 (2019).

[14] D. Baresch and V. Garbin, Acoustic trapping of microbubbles in complex environments and controlled payload release, Proc. Natl. Acad. Sci. U. S. A. **117**, 15490 (2020).

[15] A. Marzo, S. A. Seah, B. W. Drinkwater, D. R. Sahoo, B. Long, and S. Subramanian, Holographic acoustic elements for manipulation of levitated objects, Nat. Commun. **6**, 8661 (2015).

[16] A. Marzo, M. H. Caleap, and B. W. Drinkwater, Acoustic Virtual Vortices with Tunable Orbital Angular Momentum for Trapping of Mie Particles, Phys. Rev. Lett. **120**, 044301 (2018).

[17] X. M. Ren, Q. X. Zhou, Z. Xu, and X. J. Liu, Acoustic hook beam lens for particle trapping, Appl. Phys. Express **13**, 064003 (2020).

[18] J. F. Li, A. D. Crivoi, X. Y. Peng, L. Shen, Y. J. Pu, Z. Fan, and S. A. Cummer, Three dimensional acoustic tweezers with vortex streaming, Commun. Phys. **4**, 113 (2021).

[19] M. Baudoin, J. C. Gerbedoen, A. Riaud, O. B. Matar, N. Smagin, and J. L. Thomas, Folding a focalized acoustical vortex on a flat holographic transducer: Miniaturized selective acoustical tweezers, Sci. Adv. **5**, eaav1967 (2019).

[20] M. Baudoin, J. L. Thomas, R. Al Sahely, J. C. Gerbedoen, Z. X. Gong, A. Sivery, O. B. Matar, N. Smagin, P. Favreau, and A. Vlandas, Spatially selective manipulation of cells with single-beam acoustical tweezers, Nat. Commun. **11**, 4244 (2020).

[21] Z. H. Tian, Z. Y. Wang, P. R. Zhang, T. D. Naquin, J. Mai, Y. Q. Wu, S. J. Yang, Y. Y. Gu, H. T. Bachman, Y. S. Liang, Z. M. Yu, and T. J. Huang, Generating multifunctional acoustic tweezers in petri dishes for contactless, precise manipulation of bioparticles, Sci. Adv. **6**, eabb0494 (2020).

[22] A. Marzo, A. Ghobrial, L. Cox, M. Caleap, A. Croxford, and B. W. Drinkwater, Realization of compact tractor beams using acoustic delay-lines, Appl. Phys. Lett. **110**, 014102 (2017).

[23] M. A. B. Andrade, A. Marzo, and J. C. Adamowski, Acoustic levitation in mid-air: Recent advances, challenges, and future perspectives, Appl. Phys. Lett. **116**, 250501 (2020).

[24] S. Inoue, S. Mogami, T. Ichiyama, A. Noda, Y. Makino, and H. Shinoda, Acoustical boundary hologram for macroscopic rigid-body levitation, J. Acoust. Soc. Am. **145**, 328 (2019).

[25] S. Kondo and K. Okubo, Mid-air acoustic tweezers for non-contact pick up using multi-channel controlled ultrasonic transducer arrays, Jpn. J. Appl. Phys. **60**, SDDD16 (2021).

[26] Y. Yang, T. Ma, S. N. Li, Q. Zhang, J. Q. Huang, Y. F. Liu, J. W. Zhuang, Y. C. Li, X. M. Du, L. L. Niu, Y. Xiao, C. Z. Wang, F. Y. Cai, and H. R. Zheng, Self-navigated 3D acoustic tweezers in complex media based on time reversal, Research (Wash D C) **2021**, 9781394 (2021).

[27] F. Li, F. Y. Cai, Z. Y. Liu, L. Meng, M. Qian, C. Wang, Q. Cheng, M. L. Qian, X. Liu, J. R. Wu, J. Y. Li, and H. R. Zheng, Phononic-Crystal-Based Acoustic Sieve for Tunable Manipulations of Particles by a Highly Localized Radiation Force, Phys. Rev. Appl. **1**, 051001 (2014).

[28] G. Memoli, M. Caleap, M. Asakawa, D. R. Sahoo, B. W. Drinkwater, and S. Subramanian, Metamaterial bricks and quantization of meta-surfaces, Nat. Commun. **8**, 14608 (2017).

[29] Y. C. Luo, Y. R. Jia, J. Yao, D. J. Wu, and X. J. Liu, Enhanced fractional acoustic vortices by an annulus acoustic metasurface with multi-layered rings, Adv. Mater. Technol. **5**, 2000356 (2020).

[30] T. Wang, W. P. Li, Q. Yang, C. Y. Qiu, and Z. Y. Liu, Particle manipulation with acoustic vortex beam induced by a brass plate with spiral shape structure, Appl. Phys. Lett. **109**, 123506 (2016).

[31] R. Q. Zhang, H. L. Guo, W. Y. Deng, X. Q. Huang, F. Li, J. Y. Lu, and Z. Y. Liu, Acoustic tweezers and motor for living cells, Appl. Phys. Lett. **116**, 123503 (2020).

[32] Q. X. Zhou, J. Zhang, X. M. Ren, Z. Xu, and X. J. Liu, Multi-bottle beam generation using acoustic holographic lens, Appl. Phys. Lett. **116**, 133502 (2020).

[33] X. X. Xia, Q. Yang, H. Y. Li, M. Z. Ke, S. S. Peng, C. Y. Qiu, and Z. Y. Liu, Acoustic driven particle delivery assisted by a graded grating plate, Appl. Phys. Lett. **111**, 031903 (2017).

[34] Y. R. Jia, D. J. Wu, J. Yao, Q. Wei, Z. Xu, and X. J. Liu, Acoustic tweezing for both Rayleigh and Mie particles based on acoustic focused petal beams, Appl. Phys. Lett. **116**, 263504 (2020).

[35] X. X. Xia, Y. C. Li, F. Y. Cai, H. Zhou, T. Ma, J. P. Wang, J. Q. Wang, and H. R. Zhengc, Three-dimensional spiral motion of microparticles by a binary-phase logarithmic-spiral zone plate, J. Acoust. Soc. Am. **150**, 2401 (2021).

[36] Z. X. Gong and M. C. Baudoin, Particle Assembly with Synchronized Acoustic Tweezers, Phys. Rev. Appl. **12**, 024045 (2019).

[37] Z. X. Gong and M. C. Baudoin, Three-Dimensional Trapping and Assembly of Small Particles with Synchronized Spherical Acoustical Vortices, Phys. Rev. Appl. **14**, 064002 (2020).

[38] N. Jiménez, V. Romero-García, L. M. García-Raffi, F. Camarena, and K. Staliunas, Sharp acoustic vortex focusing by Fresnel-spiral zone plates, Appl. Phys. Lett. **112**, 204101 (2018).

[39] H. P. Zhou, J. J. Li, K. Guo, and Z. Y. Guo, Generation of acoustic vortex beam with designed Fermat's spiral diffraction grating, J. Acoust. Soc. Am. **146**, 4237 (2019).

[40] S. G. Ghebjagh and S. Sinzinger, Composite spiral multivalue zone plates, Appl. Opt. **59**, 4618 (2020).

[41] X. X. Xia, Y. C. Li, F. Y. Cai, H. Zhou, T. Ma, and H. R. Zheng, Ultrasonic tunable focusing by a stretchable phase-reversal Fresnel zone plate, Appl. Phys. Lett. **117**, 021904 (2020).

[42] S. Pérez-López, J. M. Fuster, P. Candelas, D. Tarrazó-Serrano, S. Castiñeira-Ibáñez, and C. Rubio, Bifocal ultrasound focusing using Bi-Fresnel zone plate lenses, Sensors **20**, 705 (2020).

[43] X. Jiang, J. J. Zhao, S. L. Liu, B. Liang, X. Y. Zou, J. Yang, C. W. Qiu, and J. C. Cheng, Broadband and stable acoustic vortex emitter with multi-arm coiling slits, Appl. Phys. Lett. **108**, 203501 (2016).

[44] Y. R. Jia, Q. Wei, D. J. Wu, Z. Xu, and X. J. Liu, Generation of fractional acoustic vortex with a discrete Archimedean spiral structure plate, Appl. Phys. Lett. **112**, 173501 (2018).

[45] D. C. Chen, Q. X. Zhou, X. F. Zhu, Z. Xu, and D. J. Wu, Focused acoustic vortex by an artificial structure with two sets of discrete Archimedean spiral slits, Appl. Phys. Lett. **115**, 083501 (2019).

[46] Z. X. Li, D. F. Wang, C. L. Fei, Z. H. Qiu, C. X. Hou, R. C. Wu, D. Li, Q. D. Zhang, D. D. Chen, Z. Y. Chen, W. Feng, and Y. T. Yang, The forbidden band and size selectivity of acoustic radiation force trapping, iScience **24**, 101988 (2021).

[47] P. Zhang, T. C. Li, J. Zhu, X. F. Zhu, S. Yang, Y. Wang, X. B. Yin, and X. Zhang, Generation of acoustic self-bending and bottle beams by phase engineering, Nat. Commun. **5**, 4316 (2014).

[48] See the Supplemental Material at http://link.aps.org/supplemental/10.1103/PhysRevApplied.17.064059 for the lateral ARF F_x and axial ARF F_z exerted on more PS spheres with different diameters, the influence of additional radial bars in the HAAP on the acoustic field and ARF, videos of two-dimensional and three-dimensional manipulations of a Mie particle by the AT, and videos of the trapping and rejecting behaviors of PS spheres with different sizes by the AT.